Calibration of Atomic Force Microscope soft cantilevers based on μ-LDV: metrological insight on the constitutive experimental parameters of Sader's formulas for flexural and

Measurement 264 (2026) 120260

Contents lists available at ScienceDirect

Measurement

journal homepage: www.elsevier.com/locate/measurement

# Calibration of Atomic Force Microscope soft cantilevers based on μ-LDV: metrological insight on the constitutive experimental parameters of Sader's formulas for flexural and torsional effective spring constant☆

Alessandro Schiavi [a,*], Luigi Ribotta [a], Isabella Camporeale [a,b], Andrea Giura [a], Massimo Zucco [a], Marco Pisani [a], Alessio Facello [a], Andrea Prato [a]

[a] Istituto Nazionale di Ricerca Metrologica – INRiM (Applied Metrology and Engineering Division), Turin, Italy
[b] Politecnico di Torino (Mechanical Engineering), Turin, Italy

ARTICLE INFO

*Keywords:*
metrological AFM
Sader's formula
μ -LDV
Cantilevers
Flexural and torsional spring constant
Uncertainties

ABSTRACT

This study investigates the experimental parameters relevant to the application of Sader's formulations for determining the effective flexural and torsional spring constants of compliant soft cantilevers used in Atomic Force Microscopy (AFM), including detailed uncertainty budgets. At INRiM, a significant upgrade of the metrological AFM system is currently underway, with the goal of enabling traceable and accurate characterization of material properties at the nanoscale.

While procedures ensuring metrological traceability to the International System of Units (SI) for nanoscale displacements along the lateral ($x$–$y$) and vertical ($z$) axes have already been established, an equivalent traceability chain for force measurements at the nanoscale has yet to be realized. Due to the intrinsic difficulties of achieving direct force traceability at micro- and nano-scales, an indirect approach is adopted: nanoscale forces are inferred from the calibrated spring constants of AFM cantilevers.

In this context, the elastic properties of the cantilevers are evaluated using micro-Laser Doppler Velocimetry, by analysing their fundamental flexural and torsional resonance frequencies along with the corresponding damping characteristics of free oscillations. These measurements are interpreted within the framework of Sader's theoretical model.

## 1. Introduction

Atomic Force Microscopy (AFM) is a well-established technique in materials characterization, widely employed for quantitative surface imaging and for assessing topographical, mechanical, and functional properties at the nanoscale. Its fundamental operating principle is governed by Hooke's law: interaction forces between the probe tip (mechanically coupled to a compliant cantilever) and the sample surface lead to measurable cantilever deflections. These deflections provide dimensional and mechanical information, enabling evaluation of morphological and rheological sample properties.

AFM supports a variety of operational modes. Static (contact) modes allow for direct force–deflection measurements, while force spectroscopy enables dynamic analysis of tip-sample interaction forces; in dynamic (non-contact or tapping) modes, the cantilever is oscillated at or near its resonance frequency, improving sensitivity and minimizing surface disturbance [1–4]. Moreover, in some advanced applications (e.g., for highly soft matters, such as biological tissues and cells), in which frictional (lateral) forces need to be determined, Frictional Force Microscopy or Lateral Force Microscopy (LFM) measures the torsional deformation of the cantilever during scanning, by measuring the forces parallel to the surface plane [5–8]. By analysing the force–displacement curves and fitting the indentation data to contact mechanics models (e.g., the Hertz model, or similar ones), the local mechanical properties of the investigated material sample can be achieved [9–13].

Precise determination of the effective flexural and torsional spring constants of AFM cantilevers is a critical prerequisite for the realization of a metrological Atomic Force Microscope. Such calibration enhances the accuracy of quantitative data acquired through AFM, and enables the provision of force traceability, at least until the force-scale

☆ This article is part of a special issue entitled: 'MEASUR_XXIV IMEKO World Congress' published in Measurement.

* Corresponding author.
*E-mail address:* a.schiavi@inrim.it (A. Schiavi).

https://doi.org/10.1016/j.measurement.2025.120260
Received 9 June 2025; Received in revised form 12 November 2025; Accepted 28 December 2025
Available online 31 December 2025

traceability is functionally extended down to micro- and nano-scale.

Among the various methods proposed in the literature to estimate cantilever stiffness, Sader's approach stands out as both comprehensive and widely used [14–19]. In this study, we use Sader's model as a case study, experimentally determining its key parameters and analysing the associated uncertainty and its propagation in detail.

The experimental investigation involves the characterization of the dynamic behavior, specifically the fundamental resonant frequencies and associated damping, of four commercially available soft cantilevers with different geometries. Measurements are performed using micro Laser Doppler Vibrometry (μ -LDV) for dynamic response analysis and Scanning Electron Microscopy (SEM) for dimensional characterization. Furthermore, the influence of hydrodynamic loading, due to the surrounding fluid medium, is considered. The fluid's physical parameters are evaluated in accordance with the model proposed by Rasmussen [20], allowing for correction of fluid–structure interactions in both flexural and torsional stiffness estimations.

This comprehensive analysis is intended to evaluate key assumptions underlying the traceability of AFM-based measurements, and to support the development of protocols that bridge the gap between qualitative imaging and traceable force metrology at the nanoscale [21].

### 1.1. A metrological AFM

A fully operational metrological Atomic Force Microscope (AFM) is designed to provide high-accuracy, SI-traceable quantification of material properties at the nanoscale. These systems, typically developed within National Metrology Institutes (NMIs) [22–27], support the measurement of topographical, dimensional, and morphological features of nanoscale objects, such as nanoparticles and nanostructures, both in-plane and out-of-plane.

Sub-nanometer resolution along the vertical (z) axis is achieved through interferometric techniques, which enable precise tracking of the relative position between the probe tip and the sample surface, with traceability to the SI unit of length [28–32].

Despite these advanced capabilities, the quantitative assessment of mechanical or rheological properties (based on force–displacement interactions between the cantilever and the sample) remains only partially realized. This limitation stems from the current lack of a direct metrological traceability chain for force measurements at micro- and nanoscales. To address this gap, interaction forces are inferred indirectly from the mechanical stiffness characteristics of the cantilevers, particularly their flexural and torsional spring constants [33–38].

At present, calibration of AFM cantilevers is facilitated by the Global Calibration Initiative (GCI), which integrates both Sader's analytical approach and thermal noise-based methods. This collaborative framework also includes the estimation of relative standard uncertainty, enabling inter-laboratory comparison and alignment across the global AFM user community [39–41].

In this context, INRiM is investigating a refined methodology for the individual calibration of AFM cantilevers. The approach is based on the dynamic analysis of free oscillations, utilizing micro Laser Doppler Vibrometry (μ -LDV) as a non-contact, high-resolution technique for evaluating the dynamic response and extracting elastic constants with enhanced precision.

### 1.2. Calibration of AFM cantilever

While the term *"calibration"* is widely used within the Atomic Force Microscopy (AFM) community, its application to the determination of cantilever elastic properties is not strictly metrologically appropriate. A more proper designation would be *"metrological characterization"*. Nonetheless, for consistency with established conventions in the AFM field, the term "calibration" will be used herein.

Over the past three decades, several theoretical and experimental methods have been proposed to determine the spring constant of AFM cantilevers, which serves as the basis for their mechanical calibration. These methods can be broadly classified into four primary categories:

1. Dimensional methods, which rely on precise measurement of the cantilever's geometric dimensions [42].
2. Static methods, which involve the application of known reference forces or displacements. Examples include the use of calibrated test masses affixed to the cantilever tip [43], quasi-static loading protocols [44], dual-cantilever comparison methods [45], and force compensation techniques utilizing electrostatic or electromagnetic actuation [46,47].
3. Dynamic methods, which exploit the cantilever's resonance behavior in conjunction with accurate measurements of its plan-view geometry [48]. Among these, the most commonly adopted techniques are the Sader method [14], the Cleveland method [49], and the thermal noise-based approach [50].
4. Reference materials, which are used to create arrays of uniform cross-section silicon-based rectangular cantilevers of different lengths attached to the end of a silicon handle chip similar in size and thickness to commercial AFM test cantilever chips, with highly reproducible shape and properties [51–55].

A detailed comparative evaluation of the first three techniques is beyond the scope of the present work, and readers are referred to the relevant literature for comprehensive discussions [56–60]. However, from a physical modeling standpoint, the Sader method stands out as particularly robust and well-formulated. It rigorously incorporates the boundary conditions and hydrodynamic interactions inherent to the oscillatory motion of a beam of arbitrary shape, immersed in a viscous fluid and subject to external driving forces. This level of analytical detail makes the Sader approach especially suitable for a high-precision metrological characterization. The possibility however to exploit reference materials, as reference standard for cantilever calibration, is the more recent development in the field, allowing to tune the elastic properties of the cantilever used in measurements directly in the AFM system, with referenced properties of the proposed NIST SRM 3461 Standard [55].

## 2. Methods and procedures

The flexural and torsional effective spring constant, respectively $k_{f,eff}$ and $k_{t,eff}$, of four commercial AFM soft cantilevers, depicted in Fig. 1 (a-d), are determined on the basis of Sader's method, connecting the dynamic spring constant to the dissipative properties of the cantilever at resonance.

Properly, the cantilever (a) is conceived for contact mode; cantilever (b) for several applications, including contact, non-contact, and tapping mode; cantilever (c) is applied for force curve applications and imaging; and cantilever (d) is a high aspect ratio silicon probe for higher speed imaging of bio samples in liquid.

The fundamental parameters required for the application of Sader's analytical formulations, as detailed in Sections 2.1.1 and 2.1.2, are determined through experimental procedures. Specifically, the cantilever's geometrical characteristics, namely length and width, are measured using Scanning Electron Microscopy (SEM) to ensure high spatial resolution. Concurrently, the dynamic response of the cantilevers, including their fundamental resonant frequencies and associated damping coefficients, is characterized using micro Laser Doppler Vibrometry (μ -LDV), which provides non-contact and high-precision vibrational measurements.

In addition, the influence of the fluid surrounding the cantilever, critical to accurately modeling the dynamic response, is systematically evaluated. The hydrodynamic loading, which alters both resonance and damping behavior, is accounted for by calculating the complex hydrodynamic function. This function depends on the actual test conditions,

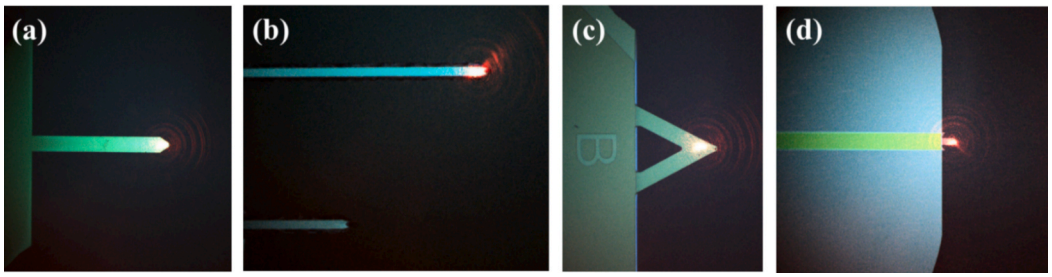


**Fig. 1.** the AFM soft cantilevers investigated in this work: (a) Nanosensor Atec Cont Au-10 [61], (b) MikroMasch XSC11 (probe A) [62], (c) Bruker NPG10 (probe B) [63], and (d) Olympus Biolever [64].

such as fluid properties (e.g., viscosity, density, temperature), as shown in Section 2.1.3.

To quantify the measurement confidence associated with the Sader-based stiffness estimation, a comprehensive uncertainty analysis is conducted. The uncertainty budgets are derived following the principles outlined in the *Guide to the Expression of Uncertainty in Measurement* (GUM) [65], using the law of propagation of uncertainty and incorporating all relevant Type A and Type B contributions.

### 2.1. Sader's method

The methods proposed by Sader, for the evaluation of flexural and torsional spring constants, is based on a direct measurement of the resonant frequency of the AFM cantilever, by monitoring its vibrations, from spectral analysis, due to thermal fluctuations. Indeed, the external driving force is simply provided by the thermal motion of air particles, inducing flexural and torsional free oscillations on the thin cantilever, as shown in Fig. 2.

From an exact scaling law, this method is applicable to arbitrary thin cantilevers (namely, rectangular and V-shaped), being the spring constants of the cantilever directly related to its mass and resonant frequency by exceedingly simple relations, independent from Young's modulus. This enables the spring constants of the different shaped cantilevers to be determined quickly and non-destructively, once the resonant frequency is known. Sader's methods development, derivation and boundary conditions analyses, are described in details in [14–19].

Theoretical background relies on the dynamic Euler-Bernoulli beam theory, and on the Euler-Lagrange equation, describing the relationship between the beam's dynamic deflection and the applied load, immersed in a viscous fluid. Sader's method provides two well-defined analytical relations, only based on experimentally measurable and verifiable quantities.

#### 2.1.1. Flexural effective spring constant

Without delving into the algebra of the analytical derivation [14–17], the fundamental generalized result of Sader for the determination of the cantilevers flexural effective spring constant $k_{f,eff}$, in N/m, converge as follows:

$$k_{f,eff} = 0.1906 b^2 L \rho_{\text{air}} \Gamma^f_{i,rect}(\omega_f) \omega_f^2 Q_f \left(\frac{L}{L - \Delta L}\right)^3, \tag{1}$$

where $b$ is the cantilever width (m), $L$ is the cantilever length (m), $\rho_{air}$ is the fluid (air) density (kg·m$^{-3}$), $\Gamma^f_{i,rect}(\omega_f)$ is the imaginary part of the hydrodynamic function for the rectangular beams, $\omega_f$ is the fundamental flexural resonance frequency of the cantilever in air (rad·s$^{-1}$), and $Q_f$ is the quality factor of the fundamental resonance frequency in air; $\Delta L$ is the distance between the center of the probe tip on the cantilever, and the end of the cantilever.

The hydrodynamic loading, due to the fluid around the cantilever, is computed by the hydrodynamic complex function for the rectangular beams $\Gamma^f_{rect}(\omega_f)$. This relation is derived from the exact analytical form of hydrodynamic complex function for circular beams $\Gamma^f_{circ}(\omega_f)$, adjusted under several assumptions, by a correction complex function $\Omega(\omega_f)$, in the following form:

$$\Gamma^f_{rect}(\omega_f) \cong \Omega(\omega_f)\Gamma^f_{circ}(\omega_f), \tag{2}$$

The hydrodynamic complex function for circular beams $\Gamma^f_{circ}(\omega_f)$, is given by:

$$\Gamma^f_{circ}(\omega_f) = 1 + \frac{4iK_1\left(-i\sqrt{i\text{Re}_f}\right)}{\sqrt{i\text{Re}_f}K_0\left(-i\sqrt{i\text{Re}_f}\right)}, \tag{3}$$

where $K_0$ and $K_1$ are the modified Bessel function of the third kind, in which the variable is $-i\sqrt{i\text{Re}_f}$, where $\text{Re}_f$ is the Reynolds number, calculated as:

$$\text{Re}_f = \frac{\rho_{\text{air}}\omega_f b^2}{4\mu_{\text{air}}}, \tag{4}$$

where $\mu_{\text{air}}$ is the fluid (air) dynamic viscosity (Pa·s), and $b$ is the width of the cantilever (assumed as the dominant length scale in the flow, i.e., for circular beams it corresponds to the diameter). The other parameters are

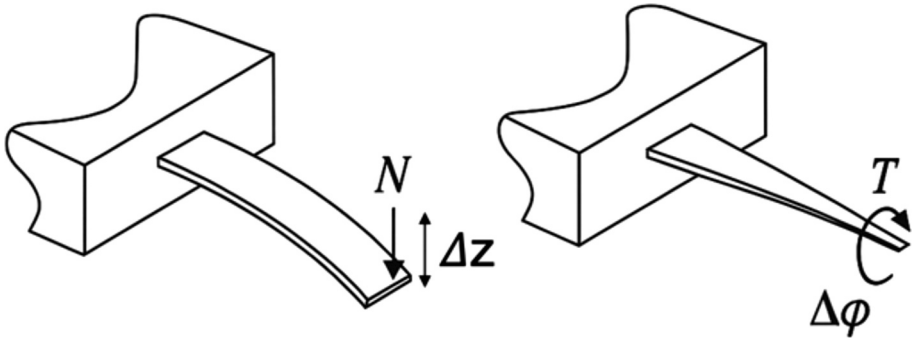


**Fig. 2.** Flexural deflection (along N-direction), and torsional deflection (around T-direction) [15].

defined in relation (1).

In order to approximate the exact analytical solution for circular beams to a suitable solution for rectangular beams, the following correction function is introduced:

$$\Omega(\omega_f) = \Omega_r(\omega_f) + i\Omega_i(\omega_f)\,, \tag{5}$$

$\Omega(\omega_f)$ is expressed as a rational function in $\log_{10}$Re, which satisfies the asymptotic conditions$\Omega(\omega_f) \to 1$ as Re $\to 0$ and Re$\to\infty$. The unknown coefficients in the rational function are evaluated from a nonlinear least-squares fit regression of sixth order function, that can be summarized as:

$$\Omega_r(\omega_f) = \left(\sum_{n=0}^{6} A_n\tau^n\right)\left(\sum_{n=0}^{6}(B_n\tau^n)^{-1}\right), \tag{6}$$

$$i\Omega_i(\omega_f) = i\left(\sum_{n=0}^{6} C_n\tau^n\right)\left(\sum_{n=0}^{6}(D_n\tau^n)^{-1}\right), \tag{7}$$

where the numerical coefficients of the fit regressions $A_n$, $B_n$, $C_n$ and $D_n$, are explicitly provided in [15], and $\tau = \log_{10}\mathrm{Re}_f$.

### 2.1.2. Torsional effective spring constant

The fundamental generalized results of Sader [18,19] for the determination of the cantilevers torsional effective spring constant $k_{t,eff}$, in N·m/rad, is:

$$k_{t,eff} = 0.1592 b^4 L \rho_{\mathrm{air}} \Gamma^t_{i,rect}(\omega_t)\omega_t^2 Q_t\left(\frac{L}{L-\Delta L}\right), \tag{8}$$

where $\Gamma^t_{i,rect}(\omega_t)$ is the imaginary part of the hydrodynamic function for the rectangular beams with respect torsional mode, $\omega_t$ is the radial resonant frequency of torsional vibration of the cantilever in air (rad·s$^{-1}$), and $Q_t$ is the quality factor of the fundamental resonance peak of torsional vibration in air; the other parameters are defined in (1). Note that the torsional spring constant depends on the forth-power of the cantilever width $b$, due to the contribution of the polar moment of inertia around the axis of rotation.

Since an analytical expression for the hydrodynamic function of a beam with a rectangular cross section undergoing torsional oscillation does not exist, the hydrodynamic torque is computed by the hydrodynamic complex function for the rectangular beams $\Gamma^t_{rect}(\omega_t)$, at the torsional resonance $\omega_t$, from the exact analytical form of hydrodynamic complex function for circular beams $\Gamma^t_{circ}(\omega_t)$, expressed as follows:

$$\Gamma^t_{circ}(\omega_t) = \frac{2i}{\mathrm{Re}_t} + \frac{iK_0\left(-i\sqrt{i\mathrm{Re}_t}\right)}{\sqrt{i\mathrm{Re}_t}K_1\left(-i\sqrt{i\mathrm{Re}_t}\right)}, \tag{9}$$

where $K_0$ and $K_1$ are the modified Bessel function of the third kind, in which the variable is $-i\sqrt{i\mathrm{Re}_t}$, where $\mathrm{Re}_t$ is the Reynolds number, calculated as shown in Eq. (4), at the corresponding torsional resonance $\omega_t$.

In this case, after some algebra, the analytical expression for the imaginary part of the hydrodynamic function for the rectangular beam in torsion, is calculated as:

$$\Gamma^t_{i,rect}(\omega_t) = \left(\frac{0.41}{\sqrt{Re_t}} + \frac{1}{Re_t}\right)\left(\sum_{n=0}^{6} E_n\tau^n\right)\left(\sum_{n=0}^{6}(F_n\tau^n)^{-1}\right), \tag{10}$$

where the numerical coefficients of the fit regression $E_n$ and $F_n$, are explicitly provided in [19], and $\tau = \log_{10}\mathrm{Re}_t$.

As is possible to notice from Eq. (1) and Eq. (8), both spring constants, $k_{f,eff}$ and $k_{t,eff}$, of the cantilever depend on two dimensional quantities, such as the width $b$, and the length $L$ (independently from thickness), and on two dynamic quantities, such as the resonance frequency of free flexural and torsional vibrations $\omega_f$ and $\omega_t$ (in air with density $\rho_{air}$), and the related quality factors $Q_f$ and $Q_t$. The effective spring constant allows to quantify forces acting on the effective position of the probe tip, with respect to the edge of the cantilever, at a certain distance $\Delta L$; in practice the load may be applied away from the end point.

It should be noted that both relation (1) and (8) also contain constant terms, namely 0.1906 and 0.1592. These terms rely to the normalized effective mass, derived from the length scale of the cantilever, as the Rayleigh quotient of the Rayleigh-Ritz method, by conservation of energy. The suitability and the "stability" of the constant terms (being length scale invariant quantities of the cantilever), have been derived and quantified according to different mathematical approaches (i.e., Green function [15] and Ritz method [66]), with identical results. It is important to underline that Sader's method accurately estimate the cantilever's stiffness even if the tip mass is quite large, but only if the first mode is used for the calibration. If for some experimental reasons, calibration should be performed on higher modes, it would be necessary to also include corrections for the tip mass [67].

### 2.1.3. Properties of air at atmospheric pressure

As expressed in Eqs. (1) and (8), the evaluation of the cantilever spring constants is inherently dependent on the physical properties of the surrounding fluid during calibration. In the present study, all calibrations are carried out in ambient air under standard atmospheric conditions. The thermophysical properties of air significantly influence the hydrodynamic functions, represented in Eqs. (3) and (9), which are critical for the accurate implementation of Sader's model.

The computation of these hydrodynamic functions, along with their associated uncertainty contributions, is a function of the Reynolds number, as defined in Eq. (4). Precise determination of air density $\rho_{\mathrm{air}}$ and dynamic viscosity $\mu_{\mathrm{air}}$ is essential, as both parameters directly affect the Reynolds number and, consequently, the resulting stiffness calculation.

To achieve this, air properties are evaluated using Rasmussen's empirical model, a formulation widely adopted in the metrological calibration of microphones [20]. This model enables accurate estimation of $\rho_{\mathrm{air}}$ and $\mu_{\mathrm{air}}$ as functions of directly measured environmental conditions, including air temperature $T$ (K), relative humidity $RH$ (%), and ambient pressure $p_0$ (Pa). The formulation accounts for the contributions of the main atmospheric constituents and their interactions, thereby enhancing the reliability of property estimation under variable laboratory conditions.

In accordance with Rasmussen's model, the air density is computed from:

$$\rho_{\mathrm{air}} = 3.48349 \bullet 10^{-3} \bullet \frac{p_s}{ZT}(1 - 0.378 \bullet x_w)\,, \tag{11}$$

and the air dynamic viscosity from:

$$\mu_{\mathrm{air}} = \left(a_0 + a_1 T + (a_2 + a_3 T)x_w + a_4 T^2 + a_5 x_w^2\right) \bullet 10^{-8}\,, \tag{12}$$

where the numerical parameters $a_n$ are explicitly provided in [20], as well as the calculation model of the mole fraction of water vapour in air $x_w$, as a function of experimental relative humidity $RH$, static pressure $p_s$, enhancement factor $f(p_s, T)$, and saturation water vapor pressure $p_{sv}(T)$; and the calculation model of compressibility factor $Z(p_s, T, x_w)$.

## 2.2. Experimental analysis

Dimensional quantities of the cantilevers are determined from SEM micrographies, as shown in Fig. 3, analysed by means of a tabletop SEM Hitachi TM3000. The images of the cantilever (measured at different magnifications 250x, 500x and 800x with an accelerating voltage of 15 kV) are analysed by extrapolating in pixels the length $L$, the width $b$, and the length $\Delta L$.

The standard deviations associated with the cantilever length $L$, width $b$, and the uncertainty in length $\Delta L$ were evaluated through

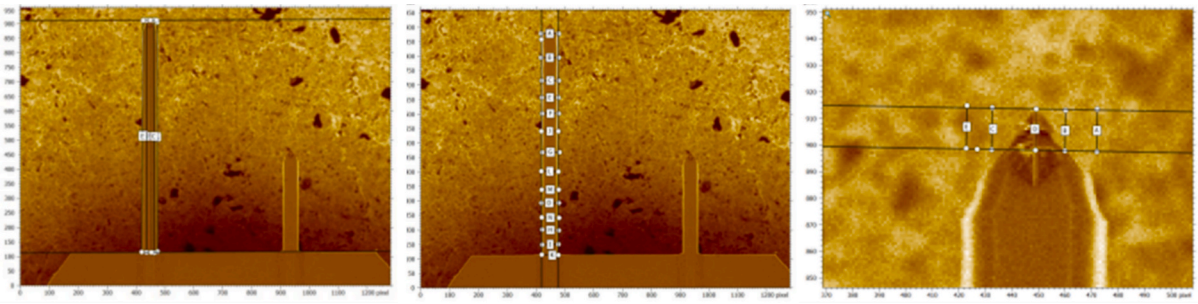

**Fig. 3.** SEM micrograph of the cantilever. Extraction of dimensional parameters: (a) length $L$, (b) width $b$, and (c) $\Delta L$ length, for the rectangular cantilever MikroMasch XSC11 (probe A).

repeated dimensional measurements. Specifically, four independent measurements of length and twenty-four of width profiles were conducted. To achieve traceable dimensional measurements, pixel calibration was performed using a certified grid reference sample (namely, line/grid SEM magnification Calibration Standard Pelcotec$^{TM}$ 633), imaged at the same magnification settings. This grid had been previously characterized using an optical diffractometer, which itself is traceable to the INRiM *MeP* frequency-stabilized He-Ne laser system, ensuring traceability to the SI. Using the calibration coefficients expressed in µm/pixel, the geometrical parameters $L$ and $b$ were accurately quantified in SI units. Dimensional data extraction and analysis were performed using *MountainsSPIP* metrology software by Digital Surf [68].

Dynamic mechanical properties were characterized through the measurement of the cantilever's fundamental flexural and torsional resonance frequencies, $\omega_f$ and $\omega_t$, as well as the corresponding quality factors, $Q_f$ and $Q_t$. These were obtained using a micro Laser Doppler Vibrometer (µ-LDV), specifically the Polytec VibroFlex Connect system, with the VibroFlex Compact sensor head, which integrates an optical camera, and both 20 × lens and 100 × lens microscope objective. The cantilever was mounted on a custom-designed fixture and the entire setup was stabilized on an active anti-vibration platform to minimize external disturbances. Resonance measurements were acquired at four discrete positions along the cantilever, with a focus near the free end (tip area), under ambient air conditions. Throughout the measurements, environmental parameters including temperature, relative humidity, and atmospheric pressure were continuously monitored and recorded in real time to ensure accurate correction of air-dependent properties.

The cantilever's frequency response was excited passively by thermal energy (i.e., Brownian motion of air molecules) eliminating the need for external excitation. It is assumed that internal energy dissipation within the cantilever structure is negligible compared to viscous damping from the surrounding medium, a condition typically valid for AFM cantilevers operating in air [50,69–72]. When viscous air damping dominates, the stochastic driving force originates primarily from molecular collisions in the surrounding air; conversely, when intrinsic material damping becomes comparable, the cantilever's internal losses contribute to the excitation. In the present case, Sader's model assumes that air damping fully governs the observed Q-factor, while internal structural damping remains negligible.

Fig. 4 presents the µ-LDV measurement configuration, including point acquisition examples on both V-shaped and rectangular cantilevers, along with the spatial locations of measurement.

The µ-LDV outputs has an analog velocity signal that is acquired by the digital oscilloscope NI PXIe-1071 (trough module NI PXIe-5114), with a sampling rate of 1 MHz. The frequency spectrum is analysed by computing a series of Fast Fourier Transform (FFT), averaged 1000 times, on $10^5$ points and has a resolution of 10 Hz. The FFT is performed using a 0.1 s Hanning-windowed dataset with 50 % overlap, ensuring minimal spectral leakage, as recommended by Sader et al. [73].

The system calibration was verified against the manufacturer's reference interferometer ($\lambda = 633$ nm). Although no specific calibration is required, according to [74] (as currently used as reference in BIPM Key Comparisons in vibration calibration), further verifications are performed according comparison procedures [75,76]. Frequency traceability is ensured by the internal rubidium-disciplined oscillator of the NI PXIe-1071 acquisition system, with fractional frequency uncertainty $< 10^{-6}$. Data-processing accuracy was verified by reproducing a reference sinusoidal excitation of known frequency and amplitude with a signal generator; the measured deviation was $< 0.01$ %.

As described below in Section 2.3, the combined contribution of the acquisition and FFT chain to the stiffness uncertainty is negligible with respect to the experimental dimensional and dynamic uncertainties.

The standard deviation of frequencies $\omega_f$ and $\omega_t$, and quality factors, $Q_f$ and $Q_t$, are calculated on the basis of 1000 averaged spectra, measurement are repeated four times, in different positions, close to the tip.

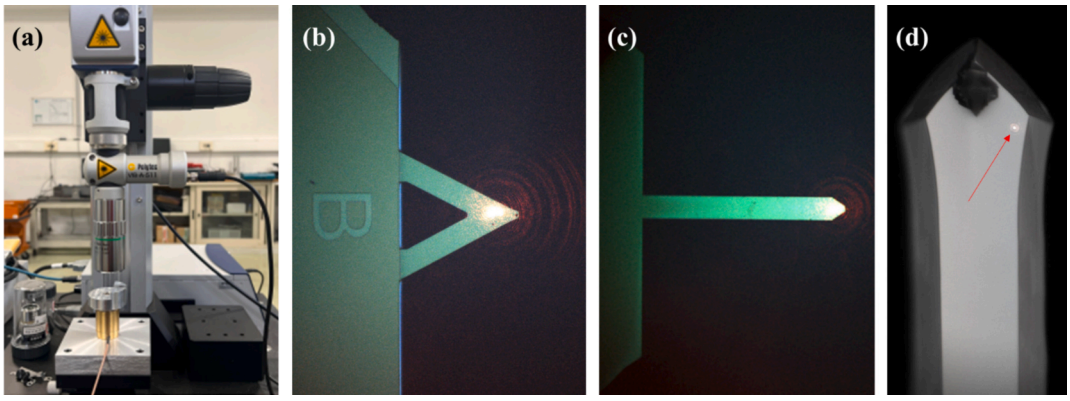


**Fig. 4.** The µ-LDV setup (a), and a single point measurement (laser spot diameter ~1.5 µ) on the a V-shaped cantilever (b) and a rectangular cantilever (c), with 20 × objective. Location of laser spot measurement positioning (d), with 100× objective.

In Fig. 5, as an example, the whole averaged thermal noise spectrum, related to a single point measurement on the cantilever (MikroMasch XSC11, probe A), along with details of the experimental flexural (13690 Hz) and torsional (335760 Hz) resonance frequencies, are shown. As is possible to notice, the resonant peaks and their widths, are clearly defined (10 Hz of resolution). It should also be noted the peaks related to the 2nd mode (86.5 kHz), and to the 3rd mode (243.8 kHz), of the flexural resonance. The torsional resonance frequency can only be detected as close as possible to the lateral edges of the cantilever, as shown in Fig. 4 (d), in which the amplitude of the torsional oscillation reaches its maximum value.

### 2.3. Uncertainty budget definition

A comprehensive evaluation of the uncertainty budget is essential for enhancing the accuracy and reliability of spring constant determinations in AFM cantilevers, thereby reinforcing the current framework for provisional force traceability at the nanoscale. Such analysis is expected to support traceability in the absence of a direct SI realization of force at this scale. The detailed uncertainty evaluation associated with the application of Sader's formulations, specifically Eqs. (1) and (8), is conducted in accordance with the *Guide to the Expression of Uncertainty in Measurement* (GUM) [65]. The related expanded uncertainty, with a confidence level of 95 % (coverage factor $k = 2$) of the spring constant $U(k_{f,eff})$, is determined as follows:

$$U(k_{f,eff}) = 2\sqrt{\sum_{i=1}^{N}\left(\frac{\partial k_{f,eff}}{\partial x_i}\right)^2 u^2(x_i)} \tag{13}$$

where $x_i$ is the $i^{th}$ independent variable of Sader's formula, and $u^2(x_i)$ is the standard uncertainty associated to the independent variable $x_i$. The identical approach is applied to calculate $U(k_{t,eff})$, to be associated to the effective torsional spring constant $k_{t,eff}$.

Each single constitutive parameter of Sader's formula, is individually expressed with the related uncertainty $u(x_i)$, the coefficient of sensitivity $\left(\frac{\partial k_{f,eff}}{\partial x_i}\right)$, and the resulting squared combined uncertainty $u_c^2(y) = \left(\frac{\partial k_{f,eff}}{\partial x_i}\right)^2 u^2(x_i)$.

The values of squared standard uncertainties, $u^2(x_i)$, are calculated either as the square of the experimental standard deviation if the quantity randomly varies (type A uncertainty), or as the square of half-width of the variability interval (divided by 3, considering a rectangular distribution) if the quantity is obtained from the manufacturer's specifications and calibration certificates (type B uncertainty).

As previously described, both the geometrical and dynamic parameters of the cantilevers are assessed through repeated measurements, to assess their inherent variability. Accordingly, the associated uncertainties are classified as Type A, in line with statistical evaluation methods.

In contrast, uncertainties linked to the ambient air properties, namely the physical characteristics of the fluid medium in which the cantilever operates, are treated as Type B uncertainties. These are propagated based on the specified performance and resolution of the monitoring instruments used during the experiment. Specifically, the air temperature ($T$), relative humidity ($RH$), and static atmospheric pressure ($p_s$) are each taken from instruments calibrated to known standards, and their associated uncertainties reflect the limitations of the measurement resolution, and manufacturer specifications.

The uncertainties related to the air properties, specifically air density $\rho_{air}$ and air dynamic viscosity $\mu_{air}$, are propagated to estimate the Reynolds's number, Eq. (5), that, in turn, allows to calculate the uncertainty associated with the hydrodynamic function $\Gamma^f_{circ}(\omega_f)$, Eq. (3), and the variability of the correction function $\Omega(\omega_f)$, Eqs. (5), (6) and (7), for the approximation to the hydrodynamic function for the rectangular beams, $\Gamma^f_{rect}(\omega_f) \cong \Omega(\omega_f)\Gamma^f_{circ}(\omega_f)$, Eq. (2). In particular, the sensitivity coefficients for both the hydrodynamic function and correction function were obtained by a simple computational numerical method (implemented by Matlab®). These were numerically calculated, by applying the limit definition of a derivative, i.e. $\lim_{d\mathrm{Re}\to 0} d(\Gamma^f_{i,rect})/d\mathrm{Re}$, where an infinitesimal Reynolds number quantity $d\mathrm{Re} = u(\mathrm{Re})/100$ is imposed, and $d\left(\Gamma^f_{i,rect}\right) = \Gamma^f_{i,rect}(\mathrm{Re}+d\mathrm{Re}) - \Gamma^f_{i,rect}(\mathrm{Re})$, from Eq. (2) and following equations, are found.

Similarly, uncertainties of air properties, at the torsional resonance $\omega_t$, are propagated to estimate the variability of the imaginary part of the hydrodynamic function for the rectangular beams with respect torsional mode $\Gamma^t_{i,rect}(\omega_t)$, Eq. (10).

In the following flow diagram, the complete set of relationships, among all the constituent parameters of Sader's formulas, along with Rasmussen's model, are summarized:

As illustrated in the flow diagram presented in Fig. 6, the experimentally acquired input quantities are identified within the green boxes. The environmental variables, specifically air temperature $T$,

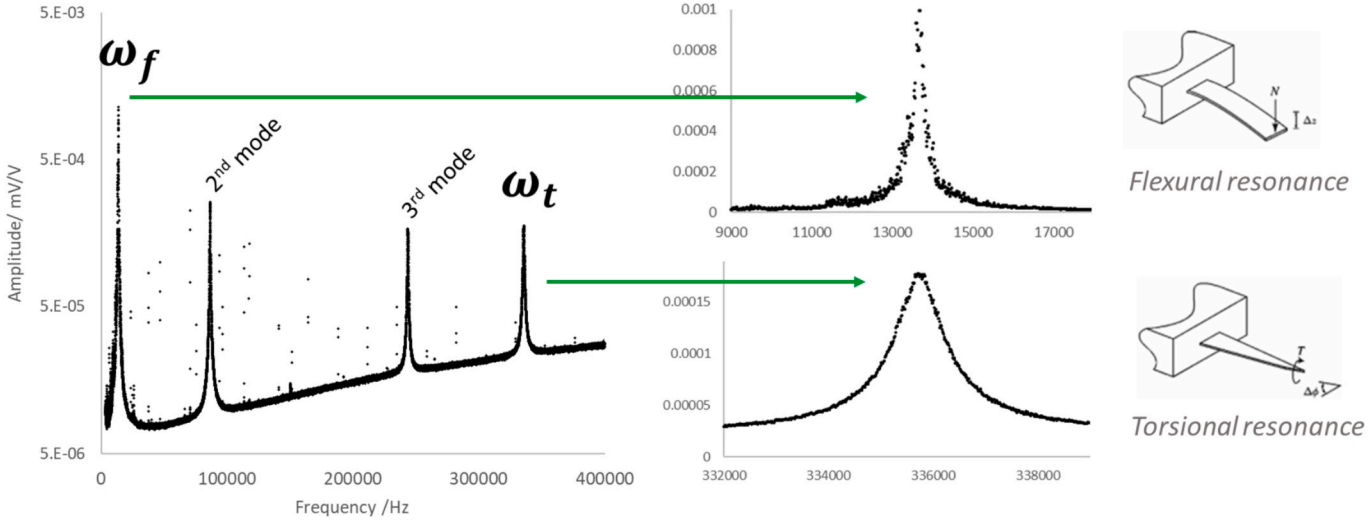


**Fig. 5.** The frequency response of the cantilever (MikroMasch XSC11, probe A), thermally excited, extracted from draft data of frequency analysis, in a single measurement point, close to the edge of the cantilever tip.

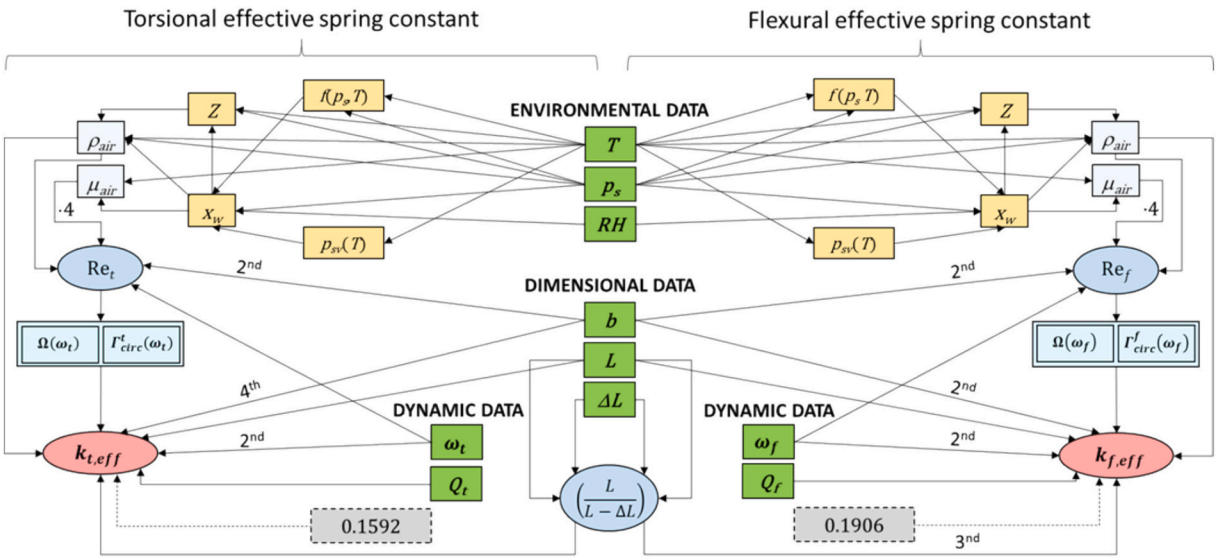


**Fig. 6.** Full flow diagram of Sader's parameters relationships.

atmospheric pressure $p_s$, and relative humidity *RH,* are used to compute the air density $\rho_{\text{air}}$ and dynamic viscosity $\mu_{\text{air}}$, incorporating the thermophysical properties of the constituent gases, as discussed in the preceding sections. The measurements were carried out under controlled laboratory climatic conditions: air temperature and relative humidity were measured, near the measuring system, using a calibrated digital thermos-hygrometer, with a resolution of 0.1 °C and 10 %, respectively, while atmospheric pressure was measured by a barometer, with a resolution of 50 Pa. The relative uncertainty (type B half-width) in percentage was calculated as the ratio between the resolution value, divided by $\sqrt{3}$ (i.e., the standard uncertainty), and the measured value. The relative uncertainty values are 0.25 % for temperature, 0.03 % for pressure, and 5.8 % for humidity, respectively. Based on these uncertainties, the extended uncertainty, according to GUM [65], for the density and dynamic viscosity was calculated using the Rasmussen model, as reported in Table 2. As can be seen, the values of the environmental parameters, although measured with instruments with not particularly fine resolution, have a small influence on the values of the thermodynamic properties. In particular, the influence of humidity is almost negligible. Uncertainties were propagated according to GUM rules, and the results (Table 2) agree within 0.05 % with the air-property uncertainties reported by Rasmussen.

These input quantities are then subjected to uncertainty propagation to determine the expanded uncertainty of the Reynolds number. Additionally, the uncertainty associated with air density is propagated directly into the computation of the cantilever's effective spring constant.

Dimensional parameters, such as the cantilever length $L$ and width $b$, contribute to the uncertainty budget of the spring constant, with width $b$ also influencing the Reynolds number estimation. Similarly, among the dynamic parameters, the uncertainty in the quality factor contributes exclusively to the spring constant evaluation, whereas the resonance frequency uncertainty is propagated to both the Reynolds number and the spring constant.

Once the expanded uncertainty of the Reynolds number is established for both flexural and torsional modes, the corresponding uncertainties in the hydrodynamic functions, referenced in Eqs. (2) and (10), are computed accordingly. The complete set of uncertainties related to the input parameters of Sader's model is subsequently propagated to yield the expanded uncertainties of the effective flexural and torsional spring constants, $k_{f,eff}$ and $k_{t,eff}$, respectively.

The detailed analysis of the coefficient of sensitivities, for each single parameter, is presented in Section 3.

## 3. Results and discussion

The experimental parameters (indicated in green boxes in the flow diagram of Fig. 6) are summarized in Table 1, with related uncertainty, type of uncertainty and percentage. The frequency $f_f$ and $f_t$ are expressed in Hz, namely the angular frequency is simply calculated by multiplying by $2\pi$, while the environmental temperature $T$ is expressed in °C, then the temperature in Kelvin is calculated by adding 273.15 K.

Here, in order to simplify the discussion, we show experimental data, uncertainties, and the related propagation, of a single cantilever (MikroMasch XSC11, probe A), as an example. In Appendix A (Table A.1, Table A.2, and Table A.3), experimental data of the other tested cantilevers are reported.

As an initial step, and in accordance with the guidelines set out in the GUM [60], the combined standard uncertainties of air density and dynamic viscosity are evaluated by analytically deriving the Rasmussen model with respect to its independent input variables, as defined in Eq. (11) and Eq. (12). This approach enables the propagation of uncertainty contributions from temperature, pressure, and relative humidity into the computed air properties. The resulting values for air density and viscosity, along with their associated standard uncertainties, are summarized in Table 2.

The uncertainties associated with the cantilever's dimensional parameters were evaluated through repeated measurements of length and width, conducted via Scanning Electron Microscopy (SEM). These repetitions enabled the estimation of Type A standard uncertainties, reflecting the inherent variability of the measurement process.

For dynamic parameters, uncertainty estimation was based on four independent measurements performed near the free end (tip) of the

**Table 1**
MikroMasch XSC11, probe A: Experimental parameters and uncertainties.

| | Value | Unit | Standard Unc. | Type | % |
|---|---|---|---|---|---|
| $T$ | 21.0 | °C | $5.8{\cdot}10^{-2}$ | B | 0.27 |
| $p_s$ | 98,890 | Pa | 28.87 | B | 0.03 |
| $RH$ | 54.6 | % | 3.15 | B | 5.77 |
| $b$ | $3.67{\cdot}10^{-5}$ | m | $1{\cdot}10^{-6}$ | A | 2.61 |
| $L$ | $52.2{\cdot}10^{-5}$ | m | $2.9{\cdot}10^{-6}$ | A | 0.55 |
| $\Delta L$ | $1.0{\cdot}10^{-5}$ | m | $2.2{\cdot}10^{-7}$ | A | 2.1 |
| $f_f$ | 13689.4 | Hz | 2.88 | B | 0.02 |
| $Q_f$ | 65.9 | – | 17.5 | B | 26.6 |
| $f_t$ | 335763.6 | Hz | 2.88 | B | 0.003 |
| $Q_t$ | 358.9 | – | 104.2 | B | 27.0 |

**Table 2**
Uncertainty budget of air density and air viscosity.

| | Value ($x_i$) | Unit | $u(x_i)$ | % |
|---|---|---|---|---|
| $\rho_{air}$ | 1.16545 | $kg{\cdot}m^{-3}$ | $5.4{\cdot}10^{-4}$ | 0.05 |
| $\mu_{air}$ | $1.81705{\cdot}10^{-5}$ | Pa·s | $3.1{\cdot}10^{-9}$ | 0.02 |

cantilever, as illustrated in Fig. 4(d). The resonance frequency showed high repeatability and stability across repetitions, indicating minimal sensitivity to positional variations, as shown in Fig. 7(a). In contrast, the quality factor, computed as $Q_f = f_f/\Delta f_{-3dB}$, exhibited greater variability, both in terms of repeatability and measurement precision.

As evidenced in Figs. 7(a) and 7(b), the estimation of the quality factor is influenced by several factors, including the spatial location of the measurement along the cantilever, the signal-to-noise characteristics of the spectral data, and to the instrumental noise. Actually, the quality factor is independent from the spatial location (in which is determined), and the observed variation are only due to the occurring background noise, that apparently "alters" the width of the resonant peak. Notably, the amplitude of the resonance peak increases progressively toward the cantilever tip, consistent with the boundary conditions of a clamped-free beam. This trend seems to be also reflected in the quality factor, which shows a corresponding apparent increase near the free end, as seen in Fig. 7(a).

To further investigate this behavior, an analysis of the cantilever's dynamic response as a function of measurement position was performed. Both resonance frequency and quality factor were extracted by fitting the measured spectral data with a Lorentzian function. Results indicate that the resonance frequency remains essentially invariant between the tip and mid-span positions, while the quality factor exhibits a position-dependent variation of approximately 10 % or more. This evidence shows that the repeatability related to the quality factor, "apparently" depends on the point of measurement, and it could greatly affect the experimental results, if not accurately taken into account. Given this evidence, we calculated the quality factor $Q_f$ solely from spectra measured on a small area at the end of the tip, using the half-power method from experimental raw data instead of a Lorentzian fit, as shown in Fig. 7(b).

Nevertheless, it is not possible to accurately establish $A_{MAX}$, (then the corresponding half-power points), and the intersection points to uniquely evaluate the width of $\Delta f_{-3dB}$, from raw data, as shown in the graph (b) of Fig. 7. Since the resonance peak is extremely narrow, even small deviations on amplitude $dA$, and on frequency $df$, lead to large variations in the estimation of the actual width of the resonance peak.

To avoid effects due to the thermal noise spectra [73], Sader suggested to use a formula allowing to calculate the true quality factor $Q_{f,true}$ allowing to reduce the uncertainty of about one order of magnitude [77], by applying the following relation:

$$Q_{f,\text{true}} = \frac{\pi f_f}{2\delta f}\left(1 - \sqrt{1 - Q_f \frac{4\delta f}{\pi f_f}}\right), \tag{14}$$

where $\delta f$ is the frequency division from the discrete Fourier transform. By analogy in torsion, $Q_{t,\text{true}}$ is calculated.

The uncertainties of the experimental parameter are then exploited to evaluate the uncertainty of the Reynolds numbers, and consequently, to propagate the uncertainties into the imaginary part of the hydrodynamic functions for the rectangular beams, calculated according Eqs. (2) and (9). Values are reported in the following Table 3.

Once the whole set of experimental data, along with uncertainties, and the related propagation into hydrodynamic function is known, it is possible to calculate the flexural and torsional effective spring constants $k_{f,eff}$ (in N/m) and $k_{t,eff}$ (in N·m/rad), of the cantilever, along with the proper expanded uncertainties.

As an example, in the following Table 4 and Table 5, the detailed uncertainty budget, including the associated squared standard uncertainty, $u^2(x_i)$, the coefficients of sensitivity, $\frac{\partial k_{f,eff}}{\partial x_i}$, and the squared combined uncertainty of the spring constants,

$u_c^2(k_{f,eff})$, of the investigated cantilever (MikroMasch XSC11, probe A), as described in Section 2.3, are shown. In addition, the graph of the draft data of measured resonances are also shown.

As shown in Table 4 and Table 5, the resulting flexural effective spring constant is $k_{f,eff} = (0.231 \pm 0.032)$ N/m, and the torsional effective spring constant of the cantilever investigated is $k_{t,eff} = (1.89 \pm 0.43) \bullet 10^{-8}$ N·m/rad. The expanded uncertainty (calculated by taking into account all possible sources of uncertainties, at a confidence level of 95 %), indicates that the flexural effective spring constant of this AFM cantilever can be accurately determined within 14 %, and within 24 % for the torsional effective spring constant.

As is possible to notice, according to the detailed budget of uncertainty, the contributions having the greatest influence on the measurement of the flexural effective spring constant $k_{f,eff}$, are mainly related to the determination of the true quality factor $Q_{f,true}$, to the width of the cantilever $b$, and to the hydrodynamic functions. As shown in Table 3, the uncertainties of the hydrodynamic functions, mainly depend on the

**Table 3**
MikroMasch XSC11 (probe A): Uncertainty budget of Reynolds numbers and of imaginary part of the hydrodynamic functions.

| | Value ($x_i$) | $u(x_i)$ | % |
|---|---|---|---|
| $Re_f$ | 1.86 | 0.10 | 5.38 |
| $Re_t$ | 48.61 | 2.38 | 4.90 |
| $\Gamma^f_{i,rect}(\omega_f)$ | 2.85 | $9.2{\cdot}10^{-2}$ | 3.21 |
| $\Gamma^t_{i,rect}(\omega_t)$ | 0.066 | $8.7{\cdot}10^{-3}$ | 13.18 |


**Fig. 7.** (a) Experimental values of the cantilever resonance peaks (fitted by Lorentzian functions), determined at different positions along the cantilever; (b) method applied for quality factor estimation (from experimental data).

**Table 4**
MikroMasch XSC11 (probe A): Detailed uncertainty budget of the flexural effective spring constant of the investigated cantilever.

| | Value $(x_i)$ | $u^2(x_i)$ | $\left(\frac{\partial k_{f,eff}}{\partial x_i}\right)$ | $u_c^2(k_{f,eff})$ | Graph of the measured flexural resonance |
|---|---|---|---|---|---|
| $b$ | $3.67\cdot10^{-5}$ | $9.2\cdot10^{-13}$ | $8.8\cdot10^{3}$ | $7.1\cdot10^{-5}$ | |
| $L$ | $52.2\cdot10^{-5}$ | $8.3\cdot10^{-12}$ | $3.1\cdot10^{2}$ | $7.9\cdot10^{-7}$ | |
| $\Delta L$ | $1.03\cdot10^{-5}$ | $8.3\cdot10^{-12}$ | $1.0\cdot10^{3}$ | $8.4\cdot10^{-6}$ | |
| $\rho_{air}$ | 1.16545 | $2.9\cdot10^{-7}$ | $1.4\cdot10^{-1}$ | $5.6\cdot10^{-9}$ | |
| $f_f$ | 13689.4 | 40 | $2.4\cdot10^{-5}$ | $2.2\cdot10^{-7}$ | |
| $Q_{f,true}$ | 65.9 | 0.25 | $2.4\cdot10^{-3}$ | $1.5\cdot10^{-6}$ | |
| $\Gamma^{f}_{rect}(\omega_f)$ | 2.85 | $8.4\cdot10^{-3}$ | $7.6\cdot10^{-1}$ | $4.9\cdot10^{-5}$ | |
| $\boldsymbol{k_{f,eff}}$ | **0.231** | | | | |
| Variance: $\sum u_c^2(k_{f,eff})$ | | | | $2.6\cdot10^{-4}$ | |
| Uncertainty: $\sqrt{\sum u_c^2(k_{f,eff})}$ | | | | $1.6\cdot10^{-2}$ | |
| Degrees of freedom: | | | | 33 | |
| Confidence level: | | | | 95.0 % | |
| Coverage factor $k$: | | | | 2.0 | |
| **Expanded uncertainty:** $k \bullet u(k_{f,eff})$ | | | | **0.032** | |

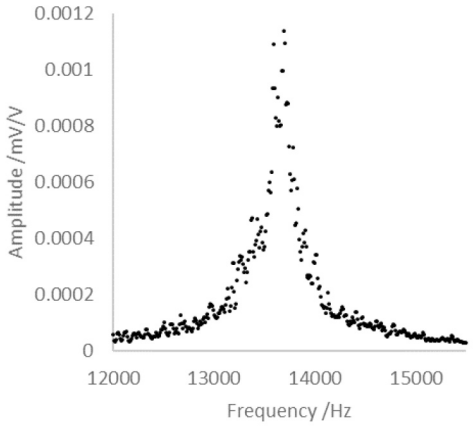


**Table 5**
MikroMasch XSC11 (probe A): Detailed uncertainty budget of the torsional effective spring constant of the investigated cantilever.

| | Value $(x_i)$ | $u^2(x_i)$ | $\left(\frac{\partial k_{t,eff}}{\partial x_i}\right)$ | $u_c^2(k_{t,eff})$ | Graph of the measured torsional resonance |
|---|---|---|---|---|---|
| $b$ | $3.67\cdot10^{-5}$ | $9.2\cdot10^{-13}$ | $2.0\cdot10^{-3}$ | $3.7\cdot10^{-18}$ | |
| $L$ | $52.2\cdot10^{-5}$ | $8.3\cdot10^{-12}$ | $3.5\cdot10^{-5}$ | $1.0\cdot10^{-20}$ | |
| $\Delta L$ | $1.03\cdot10^{-5}$ | $4.8\cdot10^{-14}$ | $3.7\cdot10^{-5}$ | $6.3\cdot10^{-23}$ | |
| $\rho_{air}$ | 1.16545 | $2.7\cdot10^{-7}$ | $1.6\cdot10^{-8}$ | $5.5\cdot10^{-24}$ | |
| $f_t$ | 335763.4 | 40 | $1.1\cdot10^{-13}$ | $4.9\cdot10^{-24}$ | |
| $Q_{t,true}$ | 358.9 | $2.2\cdot10^{-2}$ | $5.2\cdot10^{-11}$ | $5.9\cdot10^{-23}$ | |
| $\Gamma^{t}_{rect}(\omega_t)$ | 0.066 | $6.3\cdot10^{-6}$ | $2.8\cdot10^{-7}$ | $5.2\cdot10^{-20}$ | |
| $\boldsymbol{k_{t,eff}}$ | $\mathbf{1.89\cdot10^{-8}}$ | | | | |
| Variance: $\sum u_c^2(k_{t,eff})$ | | | | $3.9\cdot10^{-19}$ | |
| Uncertainty: $\sqrt{\sum u_c^2(k_{t,eff})}$ | | | | $6.3\cdot10^{-10}$ | |
| Degrees of freedom: | | | | 44 | |
| Confidence level: | | | | 95.0 % | |
| Coverage factor $k$: | | | | 2.0 | |
| **Expanded uncertainty:** $k \bullet u(k_{t,eff})$ | | | | $\mathbf{0.43\cdot10^{-8}}$ | |

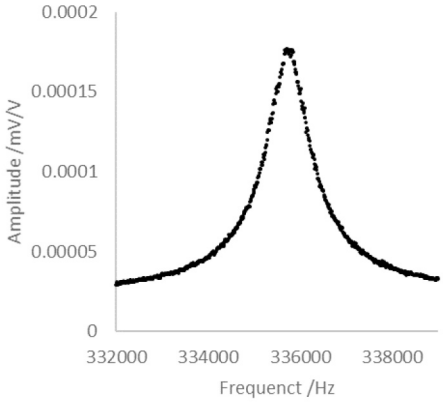


uncertainty of the Reynolds number, that depends in turns from the square of the cantilever width $b$. The evaluation of $Q_{f,true}$ is also affected by a low repeatability, as a consequence in-depth investigations of methods to mitigate the related dispersion are needed. The measurement of the torsional effective spring constant $k_{t,eff}$, is affected by similar uncertainties, with a predominance of the uncertainty due to the cantilever width (being a fourth-power quantity). In Table 6 the values of the effective elastic constants are shown, along with expended uncertainties, for the four cantilevers here investigated.

As a first approximation, the spring constant of V-shaped cantilevers (namely, Bruker NPG10 (probe B) [58]), has been calculated here by applying Eqs. (1) and (8), in that form. However, it is important to underline that some considerations on the boundary conditions are needed, in particular relating to the hydrodynamic function, Eqs. (3) and (9), to the correction factors, from Eq. (5) to Eq. (7) and Eq. (10), and to the effects on the corresponding Reynolds number, Eq. (4), for these types of cantilevers, since the peculiar shape. In particular, the hydrodynamic function, Eq. (2), follows a power-law in this form

**Table 6**
Experimental values of the effective flexural and torsional spring constants of the tested cantilevers.

| | Flexural spring constant | | | Torsional spring constant | | |
|---|---|---|---|---|---|---|
| Type of cantilever | $k_{f,eff}$/N/m | $U(k_{f,eff})$/N/m | $W(k_{f,eff})$/% | $k_{t,eff}$/N·m/rad | $U(k_{t,eff})$/N·m/rad | $W(k_{t,eff})$/% |
| MikroMasch XSC11 (probe A) | 0.231 | 0.032 | 14.1 | $1.89\cdot10^{-8}$ | $0.43\cdot10^{-8}$ | 22.8 |
| Atec Cont Au-10 | 0.208 | 0.020 | 9.6 | $1.43\cdot10^{-8}$ | $0.26\cdot10^{-8}$ | 18.4 |
| Olympus Biolever | 0.112 | 0.007 | 6.3 | $9.79\cdot10^{-11}$ | $0.73\cdot10^{-11}$ | 7.4 |
| Bruker NPG10 (probe B) | 0.176 | 0.013 | 7.4 | $6.86\cdot10^{-9}$ | $0.71\cdot10^{-9}$ | 10.4 |

$\Gamma^{f}_{rect}(\omega_f) \cong a\mathrm{Re}_f^{-0.7}$, where the coefficient $a$ depends on the plan view geometry of the device model in question. These corrections, leading to systematic effects, do not have a substantial impact on the experimental results showed in Table 6, nevertheless for a more specific analysis and their accurate quantification, the reader can refer to [17].

Similarly, some considerations must be made regarding the determination of the cantilever spring constant (d) (namely, Olympus Biolever [64]). In this case, as a first approximation, the cantilever shape was considered purely rectangular, therefore the SEM measurements refer to this form. However, this particular cantilever, as specifically explained in [78], presents two factors that complicate the determination of the cantilever length by SEM methods. The first is that the base of the cantilever is not, strictly speaking, an ideally fixed beam. Therefore, it would be necessary to take into account the compliance of the base. Furthermore, an undercut area is often present at the base of cantilevers. This has the dual effect of exacerbating the aforementioned base compliance and modifying the free length of the cantilever, so the approximation to an ideal rectangular beam leads to some further systematic effects, not taken into account in this approach.

### 3.1. Some experimental implications on the sideline

Although the measurement of the vibrational frequency response (and consequently, the flexural and torsional stiffness) is affected by both thermal effects [79–81], due to the persistence of the laser spot on the cantilever during calibration, and laser radiation pressure, which induces a certain deflection (in particular on long cantilevers) [82–84], similar conditions also occur in the operational procedures of the AFM (in which the cantilever is subjected to very similar stresses, by assuming a laser power of ~1 mW). Therefore, it can be argued that the elastic constants determined in calibration, as described above, are effectively very close (or identical) to those in operating condition.

It should also be noted that the spring constants, determined by dynamic methods, may differ from the spring constants determined by static (or quasi-static) methods, such as in tension, and so consequently, also measurements performed in static or in dynamic mode, may provide different results.

From the mechanic point of view, the difference between the static and dynamic spring constants originates from the distinct mode shapes associated with static deflection and dynamic vibration. The static stiffness is defined from the second derivative of the potential energy with respect to static displacement, while the dynamic stiffness reflects the modal curvature distribution of the vibrating beam. For the fundamental flexural mode, the two quantities differ by less than 1 % for rectangular cantilevers, as demonstrated by Sader et al. [17].

From the thermodynamic point of view, dynamic measurements are adiabatic and isentropic rather than isothermal (such as static measurements), because of failure to reach thermal equilibrium within the deformation period. However, this distinction is usually ignored, and reasonably so since the difference between adiabatic and isothermal quantities is in most cases negligible. The relationship between the static (isothermal) spring constants $k_{st}$ and the dynamic (isentropic) spring constants $k_{dyn}$, is defined by the following thermodynamic relation [85–87]:

$$k_{st} = \frac{k_{dyn}}{1 + \frac{T\alpha^2}{9\rho c_P} k_{dyn} \frac{L}{bh}}, \tag{15}$$

where $T$ is the temperature at which the cantilever is analyzed in Kelvin, $\rho$ is the density of the cantilever's material, $c_P$ is specific heat capacity at constant pressure, and $\alpha$ is the coefficient of thermal expansion; $L$, $b$, and $h$ are the dimensional parameters of the cantilever.

Silicon Nitride ($Si_3N_4$) was considered as a reference material for mechanical properties, since all analyzed cantilevers have a core made of silicon or silicon nitride. In Table 7 the range of thermophysical properties of silicon nitride are reported [88].

**Table 7**
Physical and thermal properties of silicon nitride.

| | Value ($x_i$) | Unit |
|---|---|---|
| Specific heat $c_P$ | 673 ÷ 1100 | J/(kg·K) |
| Thermal expansion coefficient $\alpha$ | 1.4 ÷ 3.7 | $10^{-6}$ K$^{-1}$ |
| Density $\rho$ | 2370 ÷ 3250 | kg/m$^3$ |
| Cantilever thickness $h$ | 1 ÷ 3 | $10^{-6}$ m |

According to parameters shown in Table 7, and by assuming a nominal thickness of 1 ÷ 3 μm (as from technical datasheets), it is possible to verify that, for all tested cantilevers, the static and the dynamic elastic constant can be considered equal, namely $k_{st} \approx k_{dyn}$, being the denominator of Eq. (15) $\approx 1 + 3 \bullet 10^{-8}$ N/m.

## 4. Conclusions

This paper deals with the update of the metrological AFM developed in INRIM, in order to provide quantitative evaluations of the rheological, mechanical and functional properties of materials at the nano-scale level, along the traceability to the International System of Units (SI). An accurate calibration method, based on Sader's methods for the determination of the flexural and torsional effective spring constants of cantilevers used in AFM, is presented. Experimental evidence and results here presented, referred to four commercial AFM soft cantilevers. The constitutive parameters of Sader's formulas, are experimentally measured, along with the proper uncertainties, and the related propagation, according to GUM rules. Dimensional quantities of the cantilever are determined from repeated measurement of length and width, by means of Scanning Electron Microscope (SEM), traceable to SI, and dynamic quantities, namely resonance frequency and quality factor, are determined from repeated measurement by using a micro Laser Doppler Velocimetry (μ-LDV) technique, traceable to SI. Moreover, the uncertainties of the hydrodynamic function (only dependent from Reynolds number) are investigated as well, by propagating the uncertainties from the Rasmussen model, applied to accurately calculate the air properties. The values of the flexural and torsional stiffness, are supplied along with the proper expanded uncertainties, by taking into account all possible sources of uncertainties. Experimental results show that the precision of elastic constants, determined according to the proposed methods, range between 7 % up to 14 % for the flexural stiffness, and between 7 % up to 23 % for the torsional stiffness.

The analysis of the uncertainty budgets, on the basis of the sensitivity coefficients, and of the related combined uncertainties, found that the main critical parameters are the quality factor, the hydrodynamic functions, and the width of the cantilevers.

The main difficulty encountered in accurately determining the quality factor depends both on the low repeatability of the measurements (which significantly depends on the point where it is detected), and on the dispersion of the data (points-cloud) that actually constitute the frequency response. The use of the "true" quality factor is claimed to reduce uncertainties due to thermal noise effects, nevertheless in depth investigation on the validity of that formulation are needed, in particular for traceable measurements of a dynamic quantity. Appropriate fitting curves can facilitate the calculation, however even the uncertainties related to the fit are not negligible, since the reconstruction of the signal, near or below the background noise, returns different fits. This is a critical point, because the observed variations of the quality factor, from draft data, can even exceed 20 %.

The uncertainties related to the measurements of dimensional quantities are mainly due to the uncertainty contribution of the used line/grid SEM magnification Calibration Standard Pelcotec™ 633 (with 2 % of expanded uncertainty) [89], calibrated by using a laser diffractometer. The use of the calibrated line/grid SEM allows us to obtained dimensional measurements traceable to SI. The measurements of

dimensional quantities are expected to be improved by using more performing SEM instrument, and a more detailed line/grid SEM magnification Calibration Standard, in order to better characterize the pixel size, and at the same time, to provide traceable measurements.

The uncertainty due to the hydrodynamic functions, directly depends on the uncertainty of the cantilever width, being functions of Reynolds numbers. The effects of the cantilever width uncertainty strongly affect the torsional stiffness, being dependant from the fourth-power. So it is expected that by improving the measurements and the experimental methods for the determination of the quality factor and the cantilever width, it would be possible to greatly reduce the expanded associated uncertainties, and consequently enhancing the traceability of the micro- and nano-force, returned by the AFM measurements.

The experimental values of the flexural stiffness are in agreement with data provided by manufactures, while no information are available for the torsional stiffness. Nevertheless, according to Sader observations on similar cantilevers, results show a certain compatibility.

Future steps of these activities include both the participation in international comparisons, in order to verify the suitability of the proposed method, and the application of the metrological AFM, for the accurate evaluation of the rheological mechanical and functional properties, of materials and soft materials used in the medical and biomedical fields.

## CRediT authorship contribution statement

**Alessandro Schiavi:** Writing – review & editing, Writing – original draft, Supervision, Methodology, Investigation, Funding acquisition, Formal analysis, Conceptualization. **Luigi Ribotta:** Writing – review & editing, Writing – original draft, Validation, Methodology, Investigation, Formal analysis, Data curation. **Isabella Camporeale:** Writing – review & editing, Validation, Investigation, Formal analysis, Data curation. **Andrea Giura:** Validation, Software, Formal analysis, Data curation. **Massimo Zucco:** Writing – review & editing, Validation, Methodology, Conceptualization. **Marco Pisani:** Writing – review & editing, Supervision, Investigation, Formal analysis, Conceptualization. **Alessio Facello:** Validation, Software, Methodology, Formal analysis, Data curation. **Andrea Prato:** Writing – review & editing, Supervision, Methodology, Formal analysis, Data curation, Conceptualization.

## Declaration of competing interest

The authors declare that they have no known competing financial interests or personal relationships that could have appeared to influence the work reported in this paper.

## Acknowledgments

Project funded under the National Recovery and Resilience Plan (NRRP), Mission 04 Component 2 Investment 3.1 – NextGenerationEU, Call for tender n. 3264 dated 28/12/2021.

Award Number: 128 dated 21/06/2022 – Project Code: IR0000027 - iENTRANCE@ENL: Infrastructure for Energy TRAnsition aNd Circular Economy @ EuroNanoLab.

The authors are grateful to Bruno Torre (INRIM - ML division) for providing Olympus Biolever cantilevers.

## Appendix A

**Table A1**
Experimental parameters and uncertainties of cantilever Atec Cont Au-10, and the experimental draft data of flexural (up) and torsional (down) resonance frequencies.

| | Value | Unit | Standard Unc. | Type | % | Resonance frequencies |
|---|---|---|---|---|---|---|
| $T$ | 21.1 | °C | $5.8{\cdot}10^{-2}$ | B | 0.25 | |
| $p_s$ | 98,890 | Pa | 28.87 | B | 0.03 | |
| $RH$ | 54.4 | % | 3.15 | B | 5.77 | |
| $b$ | $5.14{\cdot}10^{-5}$ | m | $1.1{\cdot}10^{-6}$ | A | 1.94 | |
| $L$ | $45.5{\cdot}10^{-5}$ | m | $1.3{\cdot}10^{-6}$ | A | 0.29 | |
| $\Delta L^*$ | 0 | m | 0 | – | 0 | |
| $f_f$ | 11,710 | Hz | 2.88 | B | 0.03 | |
| $Q_f$ | 68.92 | – | 9.39 | B | 13.6 | |
| $f_t$ | 192,070 | Hz | 2.88 | B | 0.004 | |
| $Q_t$ | 270.5 | – | 82.42 | B | 26.7 | |
| $\mathrm{Re}_f$ | 3.12 | – | 0.12 | A | 3.89 | |
| $\mathrm{Re}_t$ | 51.20 | – | 1.99 | A | 3.85 | |
| $\Gamma^f_{rect}(\omega_f)$ | 2.087 | – | 0.048 | A | 2.3 | |
| $\Gamma^t_{i,rect}(\omega_t)$ | 0.061 | – | 0.003 | A | 9.7 | |

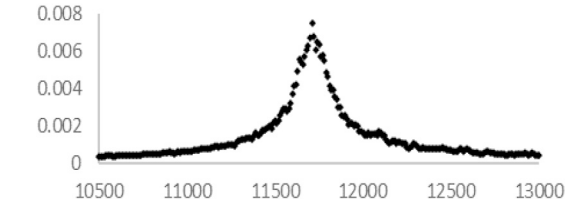


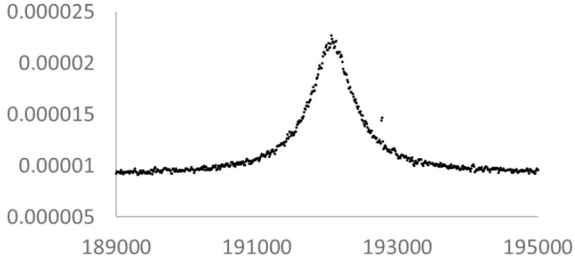


$\Delta L^*$ in this cantilever the probe tip is mounted at the end of the cantilever.

**Table A2**
Experimental parameters and uncertainties of cantilever Olympus Biolever, and the experimental draft data of flexural (up) and torsional (down) resonance frequencies.

| | Value | Unit | Standard Unc. | Type | % | Resonance frequencies |
|---|---|---|---|---|---|---|
| $T$ | 21.0 | °C | $5.8{\cdot}10^{-2}$ | B | 0.27 | |
| $p_s$ | 98,890 | Pa | 28.87 | B | 0.03 | |
| $RH$ | 54.6 | % | 3.15 | B | 5.77 | |
| $b$ | $1.75{\cdot}10^{-5}$ | m | $1.3{\cdot}10^{-7}$ | A | 0.74 | |
| $L$ | $4.14{\cdot}10^{-5}$ | m | $6.0{\cdot}10^{-8}$ | A | 0.15 | |
| $\Delta L$ | $0.39{\cdot}10^{-5}$ | m | $6.0{\cdot}10^{-8}$ | A | 1.3 | |
| $f_f$ | 98,894 | Hz | 2.88 | B | 0.003 | |
| $Q_f$ | 36.31 | – | 9.85 | B | 27.1 | |
| $f_t$ | 533,210 | Hz | 2.88 | B | 0.0005 | |
| $Q_t$ | 86.8 | – | 23.2 | B | 26.7 | |
| $\mathrm{Re}_f$ | 3.04 | – | 0.05 | A | 1.49 | |
| $\mathrm{Re}_t$ | 16.43 | – | 0.24 | A | 1.49 | |
| $\Gamma^f_{rect}(\omega_f)$ | 2.117 | – | 0.02 | A | 0.9 | |
| $\Gamma^t_{i,rect}(\omega_t)$ | 0.127 | – | 0.003 | A | 2.1 | |

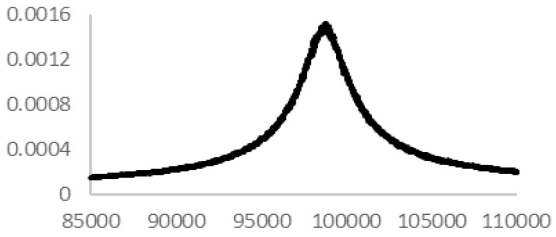


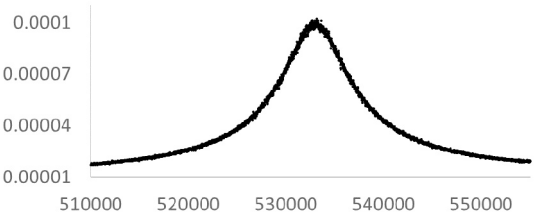


**Table A3**
Experimental parameters and uncertainties of cantilever Bruker NPG10 (probe B), and the experimental draft data of flexural (up) and torsional (down) resonance frequencies.

| | Value | Unit | Standard Unc. | Type | % | Resonance frequencies |
|---|---|---|---|---|---|---|
| $T$ | 21.1 | °C | $5.8{\cdot}10^{-2}$ | B | 0.25 | |
| $p_s$ | 98,880 | Pa | 28.87 | B | 0.03 | |
| $RH$ | 54.6 | % | 3.15 | B | 5.77 | |
| $b$ | $4.89{\cdot}10^{-5}$ | m | $5.3{\cdot}10^{-7}$ | A | 1.1 | |
| $L$ | $20.4{\cdot}10^{-5}$ | m | $5.6{\cdot}10^{-7}$ | A | 0.28 | |
| $\Delta L$ | $0.37{\cdot}10^{-5}$ | m | $5.0{\cdot}10^{-8}$ | A | 1.4 | |
| $f_f$ | 21,589 | Hz | 2.88 | B | 0.01 | |
| $Q_f$ | 53.73 | – | 14.26 | B | 26.5 | |
| $f_t$ | 261,180 | Hz | 2.88 | B | 0.002 | |
| $Q_t$ | 214.1 | – | 82.42 | B | 20.5 | |
| $\mathrm{Re}_f$ | 5.20 | – | 0.11 | A | 2.17 | |
| $\mathrm{Re}_t$ | 62.94 | – | 1.36 | A | 2.17 | |
| $\Gamma^f_{rect}(\omega_f)$ | 2.087 | – | 0.048 | A | 2.3 | |
| $\Gamma^t_{i,rect}(\omega_t)$ | 0.053 | – | 0.001 | A | 2.9 | |

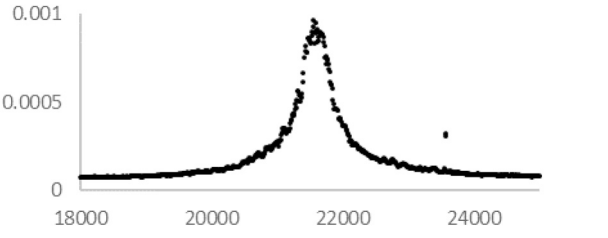


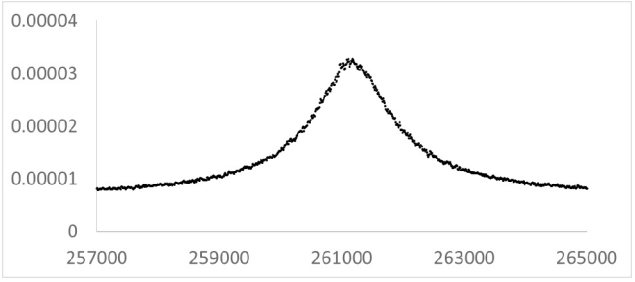


## Data availability

Data will be made available on request.

## References

[1] P. Eaton, P. West, Atomic Force Microscopy, Oxford University Press, 2010.
[2] D. Rugar, P. Hansma, Atomic force microscopy, Phys. Today 43 (10) (1990) 23–30.
[3] R. Garcia, R. Perez, Dynamic atomic force microscopy methods, Surf. Sci. Rep. 47 (6–8) (2002) 197–301.
[4] F.J. Giessibl, Advances in atomic force microscopy, Rev. Mod. Phys. 75 (3) (2003) 949.

[5] M. Munz, Force calibration in lateral force microscopy: a review of the experimental methods, J. Phys. D Appl. Phys. 43 (6) (2010) 063001.
[6] R.G. Cain, S. Biggs, N.W. Page, Force calibration in lateral force microscopy, J. Colloid Interface Sci. 227 (1) (2000) 55–65.
[7] A.M. Joshua, G. Cheng, E.V. Lau, Soft matter analysis via atomic force microscopy (AFM): a review, Appl. Surf. Sci. Adv. 17 (2023) 100448.
[8] R. Bennewitz, Friction force microscopy, in: Fundamentals of Friction and Wear on the Nanoscale, Springer International Publishing, Cham, 2024, pp. 1–16.
[9] B. Cappella, G. Dietler, Force-distance curves by atomic force microscopy, Surf. Sci. Rep. 34 (1–3) (1999) 1–104.
[10] H.J. Butt, B. Cappella, M. Kappl, Force measurements with the atomic force microscope: Technique, interpretation and applications, Surf. Sci. Rep. 59 (1–6) (2005) 1–152.
[11] S.V. Kontomaris, A. Malamou, A. Stylianou, The Hertzian theory in AFM nanoindentation experiments regarding biological samples: Overcoming limitations in data processing, Micron 155 (2022) 103228.
[12] K. Mendová, M. Otáhal, M. Drab, M. Daniel, Size matters: rethinking hertz model interpretation for cell mechanics using AFM, Int. J. Mol. Sci. 25 (13) (2024) 7186.
[13] A.C. Campbell, P. Klapetek, R. Šlesinger, V. Witkovský, G. Wimmer, Fitting the AFM force–distance curves the correct way, Meas. Sci. Technol. 36 (1) (2024) 015022.
[14] J.E. Sader, I. Larson, P. Mulvaney, L.R. White, Method for the calibration of atomic force microscope cantilevers, Rev. Sci. Instrum. 66 (7) (1995) 3789–3798.
[15] J.E. Sader, Frequency response of cantilever beams immersed in viscous fluids with applications to the atomic force microscope, J. Appl. Phys. 84 (1) (1998) 64–76.
[16] J.E. Sader, J.W. Chon, P. Mulvaney, Calibration of rectangular atomic force microscope cantilevers, Rev. Sci. Instrum. 70 (10) (1999) 3967–3969.
[17] J.E. Sader, J.A. Sanelli, B.D. Adamson, J.P. Monty, X. Wei, S.A. Crawford, E. J. Bieske, Spring constant calibration of atomic force microscope cantilevers of arbitrary shape, Rev. Sci. Instrum. 83 (10) (2012).
[18] C.P. Green, H. Lioe, J.P. Cleveland, R. Proksch, P. Mulvaney, J.E. Sader, Normal and torsional spring constants of atomic force microscope cantilevers, Rev. Sci. Instrum. 75 (6) (2004) 1988–1996.
[19] C.P. Green, J.E. Sader, Torsional frequency response of cantilever beams immersed in viscous fluids with applications to the atomic force microscope, J. Appl. Phys. 92 (10) (2002) 6262–6274.
[20] K. Rasmussen, Calculation Methods for the Physical Properties of Air Used in the Calibration of Microphones, Report No. PL-11b, Technical University of Denmark, Lyngby, Denmark, 1997.
[21] A. Schiavi, L. Ribotta, L. Bruno, M. Pisani, R. Bellotti, M. Zucco, A. Prato, Calibration of Atomic Force Microscope Cantilevers Based on μ-LDV: Metrological Insight on the Constitutive Experimental Parameters of Sader's Formula for Spring Constant, Sensors, Measurement, 2025.
[22] J.A. Kramar, R. Dixson, N.G. Orji, Scanning probe microscope dimensional metrology at NIST, Meas. Sci. Technol. 22 (2011) 11, https://doi.org/10.1088/0957-0233/22/2/024001.
[23] J. Herrmann, M. Lawn, C. Freund, J. Miles, V. Coleman, Å. Jämting, Development of a scanning probe microscope for traceable nanoscale length metrology. Proceedings of the Euspen International Conference, 2010.
[24] V. Korpelainen, J. Seppä, A. Lassila, Design and characterization of MIKES metrological atomic force microscope, Precis. Eng. 34 (2) (2010) 735–744, https://doi.org/10.1016/j.precisioneng.2010.04.002.
[25] S. Ducourtieux, B. Poyet, Development of a metrological atomic force microscope with minimized Abbe error and differential interferometer based realtime position control, Meas. Sci. Technol. 22 (2011) 15, https://doi.org/10.1088/0957-0233/22/9/094010.
[26] M. Bienias, S. Gao, K. Hasche, R. Seemann, K. Thiele, A metrological scanning force microscope used for coating thickness and other topographical measurements, Appl. Phys. A 66 (1998) 837–S842, https://doi.org/10.1007/s003390051252.
[27] G.B. Picotto, M. Pisani, A sample scanning system with nanometric accuracy for quantitative SPM measurements, Ultramicroscopy 86 (1–2) (2001) 247–254, https://doi.org/10.1016/S0304-3991(00)00112-1.
[28] G.B. Picotto, M. Vallino, L. Ribotta, Tip–sample characterization in the AFM study of a rod-shaped nanostructure, Meas. Sci. Technol. 31 (8) (2020) 084001.
[29] R. Bellotti, G.B. Picotto, L. Ribotta, AFM measurements and tip characterization of nanoparticles with different shapes, Nanomanuf. Metrol. 5 (2) (2022) 127–138.
[30] V. Maurino, F. Pellegrino, G.B. Picotto, L. Ribotta, Quantitative three-dimensional characterization of critical sizes of non-spherical $TiO_2$ nanoparticles by using atomic force microscopy, Ultramicroscopy 234 (2022) 113480.
[31] L. Ribotta, Dimensional Metrology at the Nanoscale: Quantitative Characterization of Nanoparticles by Means of Metrological Atomic Force Microscopy, PhD Dissertation, Politecnico di Torino, 2022.
[32] L. Ribotta, A. Delvallée, E. Cara, R. Bellotti, A. Giura, I. De Carlo, L. Boarino, AFM interlaboratory comparison for nanodimensional metrology on silicon nanowires, Meas. Sci. Technol. 35 (10) (2024) 105014.
[33] Y. Zheng, L. Song, G. Hu, X. Cai, H. Liu, J. Ma, F. Fang, The multi-position calibration of the stiffness for atomic-force microscope cantilevers based on vibration, Meas. Sci. Technol. 26 (5) (2015) 055001.
[34] K. Marti, C. Wuethrich, M. Aeschbacher, S. Russi, U. Brand, Z. Li, Micro-force measurements: a new instrument at METAS, Meas. Sci. Technol. 31 (7) (2020) 075007.
[35] M.S. Kim, J.R. Pratt, U. Brand, C.W. Jones, Report on the first international comparison of small force facilities: a pilot study at the micronewton level, Metrologia 49 (1) (2011) 70.
[36] G. Hu, J. Jiang, Z. Zhang, Y. Zhang, U. Brand, M.-S. Kim, Investigation of a small force standard with the mass based method, ACTA IMEKO 6 (2) (2017) 13–20.
[37] V. Nesterov, D. Nies, O. Belai, S. Buetefisch, J. Kirchhoff, M. Mueller, U. Brand, The status of PTB's nanonewton force facility, IEEE Trans. Instrum. Meas. 68 (6) (2019) 1982–1989.
[38] D.B. Newell, J.A. Kramar, J.R. Pratt, D.T. Smith, E.R. Williams, The NIST microforce realization and measurement project, IEEE Trans. Instrum. Meas. 52 (2) (2003) 508–511.
[39] J.E. Sader, in: Encyclopedia of Surface and Colloid Science, Dekker, New York, 2002, pp. 846–856.
[40] J.E. Sader, R. Borgani, C.T. Gibson, D.B. Haviland, M.J. Higgins, J.I. Kilpatrick, T. Zheng, A virtual instrument to standardise the calibration of atomic force microscope cantilevers, Rev. Sci. Instrum. 87 (9) (2016).
[41] See https://sadermethod.org for GCI, last web access May 2025.
[42] C.A. Clifford, M.P. Seah, The determination of atomic force microscope cantilever spring constants via dimensional methods for nanomechanical analysis, Nanotechnology 16 (9) (2005) 1666.
[43] M.S. Kim, J.H. Choi, Y.K. Park, J.H. Kim, Atomic force microscope cantilever calibration device for quantified force metrology at micro-or nano-scale regime: the nano force calibrator (NFC), Metrologia 43 (5) (2006) 389.
[44] L. Kumanchik, T.L. Schmitz, J.R. Pratt, An interferometric platform for studying AFM probe deflection, Precis. Eng. 35 (2) (2011) 248–257, https://doi.org/10.1016/j.precisioneng.2010.09.013.
[45] C.A. Clifford, M.P. Seah, Improved methods and uncertainty analysis in the calibration of the spring constant of an atomic force microscope cantilever using static experimental methods, Measur. Sci. Technol. 20 (2009) 125501.
[46] V. Cherkasova, Z. Li, R. Popadic, T. Froehlich, U. Brand, Calibration of the stiffness of soft cantilevers based on electromagnetic and electrostatic force compensation principles, Measurement: Sensors (2024) 101335.
[47] V. Cherkasova, T. Fröhlich, Force-Displacement Measurement System with Electromagnetic and Electrostatic Force Compensation Principles 91 (2024) 8–13.
[48] A.D. Slattery, J.S. Quinton, C.T. Gibson, Atomic force microscope cantilever calibration using a focused ion beam, Nanotechnology 23 (2012) 285704.
[49] J.P. Cleveland, S. Manne, D. Bocek, P.K. Hansma, A nondestructive method for determining the spring constant of cantilevers for scanning force microscopy, Rev. Sci. Instrum. 64, 2 (1993) 403–405.
[50] J.L. Hutter, J. Bechhoefer, Calibration of atomic-force microscope tips, Rev. Sci. Instrum. 64 (7) (1993) 1868–1873.
[51] R.S. Gates, J.R. Pratt, Prototype cantilevers for SI-traceable nanonewton force calibration, Meas. Sci. Technol. 17 (10) (2006) 2852.
[52] J.R. Pratt, G.A. Shaw, L. Kumanchik, N.A. Burnham, Quantitative assessment of sample stiffness and sliding friction from force curves in atomic force microscopy, J. Appl. Phys. 107 (4) (2010).
[53] G.A. Shaw, J. Stirling, J.A. Kramar, A. Moses, P. Abbott, R. Steiner, A. Koffman, J. R. Pratt, Z.J. Kubarych, Milligram mass metrology using an electrostatic force balance, Metrologia 53 (5) (2016) A86–A94.
[54] J. Stirling, G.A. Shaw, Realising traceable electrostatic forces despite non-linear balance motion, Meas. Sci. Technol. 28 (5) (2017).
[55] R. Gates, W. Osborn, M. McLean, G. Shaw, J. Filliben, Certification of Standard Reference Material® 3461 Reference Cantilevers for AFM Spring constant Calibration, special Publication (NIST SP), National Institute of Standards and Technology, 2022, 10.6028/NIST.SP.260-227. last access November 2025.
[56] C.T. Gibson, D.A. Smith, C.J. Roberts, Calibration of silicon atomic force microscope cantilevers, Nanotechnology 16 (2) (2005) 234.
[57] M.S. Kim, J.H. Choi, J.H. Kim, Y.K. Park, Accurate determination of spring constant of atomic force microscope cantilevers and comparison with other methods, Measurement 43 (4) (2010) 520–526.
[58] D. Georgakaki, S. Mitridis, A.A. Sapalidis, E. Mathioulakis, H.M. Polatoglou, Calibration of tapping AFM cantilevers and uncertainty estimation: Comparison between different methods, Measurement 46 (10) (2013) 4274–4281.
[59] Y. Song, S. Wu, L. Xu, X. Fu, Accurate calibration and uncertainty estimation of the normal spring constant of various AFM cantilevers, Sensors 15 (3) (2015) 5865–5883.
[60] U. Brand, S. Gao, W. Engl, T. Sulzbach, S.W. Stahl, Comparing AFM cantilever stiffness measured using the thermal vibration and the improved thermal vibration methods with that of an SI traceable method based on MEMS, Meas. Sci. Technol. 28 (3) (2017) 034010.
[61] https://www.nanosensors.com/advanced-tip-at-the-end-of-the-cantilever-contact-mode-au-coating-afm-tip-ATEC-CONTAu, last web access May 2025.
[62] https://www.spmtips.com/afm-tip-hq-xsc11-hard-al-bs, last web access May 2025.
[63] https://www.brukerafmprobes.com/p-3432-npg-10.aspx, last web access May 2025.
[64] https://estore.oxinst.com/eu/products/afm-probes/afm-probes-catalog/zid803.OLY.BL-AC40TS, last web access May 2025.
[65] JCGM 100, Evaluation of Measurement Data — Guide to the Expression of uncertainty in Measurement (GUM), Joint Committee for Guides in Metrology, Sévres, France, 2008.
[66] H. Sumali, M.S. Allen, E.B. Locke, Experimental/Analytical Evaluation of the Effect of Tip Mass on Atomic Force Microscope Calibration (No. SAND2007-7352C), Sandia National Lab.(SNL-NM), Albuquerque, NM (United States), 2007.
[67] M.S. Allen, H. Sumali, P.C. Penegor, DMCMN: experimental/analytical evaluation of the effect of tip mass on atomic force microscope cantilever calibration, J. Dyn. Syst. Meas. Contr. 131 (2009) 6.
[68] See https://www.digitalsurf.com/software-solutions/scanning-probe-microscopy/, last web access May 2025.
[69] N.T. Garabedian, H.S. Khare, R.W. Carpick, D.L. Burris, AFM at the macroscale: methods to fabricate and calibrate probes for millinewton force measurements, Tribol. Lett. 67 (2019) 1–10.

[70] Y. Tian, C. Zhou, F. Wang, K. Lu, D. Zhang, A novel compliant mechanism based system to calibrate spring constant of AFM cantilevers, Sens. Actuators, A 309 (2020) 112027.
[71] W.E. Newell, Miniaturization of Tuning Forks: Integrated electronic circuits provide the incentive and the means for orders-of-magnitude reduction in size, Science 161 (3848) (1968) 1320–1326.
[72] T.R. Albrecht, S. Akamine, T.E. Carver, C.F. Quate, Microfabrication of cantilever styli for the atomic force microscope, J. Vac. Sci. Technol. A 8 (4) (1990) 3386–3396.
[73] J.E. Sader, J. Sanelli, B.D. Hughes, J.P. Monty, E.J. Bieske, Distortion in the thermal noise spectrum and quality factor of nanomechanical devices due to finite frequency resolution with applications to the atomic force microscope, Rev. Sci. Instrum. 82 (9) (2011).
[74] J.A. Stone, J.E. Decker, P. Gill, P. Juncar, A. Lewis, G.D. Rovera, M. Viliesid, "Advice from the CCL on the use of unstabilized lasers as standards of wavelength: the helium–neon laser at 633 nm, Metrologia 46 (2009) 11–18.
[75] D. Sprecher, C. Hof, Primary accelerometer calibration by scanning laser Doppler vibrometry, Meas. Sci. Technol. 31 (6) (2020) 065006.
[76] H. Nozato, W. Kokuyama, T. Shimoda, H. Inaba, Primary calibration method for laser Doppler vibrometers using electro-optical modulator, Precis. Eng. 93 (2025) 204–215.
[77] J.E. Sader, J.R. Friend, Note: Calibration of atomic force microscope cantilevers using only their resonant frequency and quality factor, Rev. Sci. Instrum. 85 (11) (2014).
[78] https://www.nanoandmore.com/AFM-Probe-BL-AC40TS?srsltid=AfmBOooMtZkLblfMDGDYHif4bDDM6J3oARn160vjyDfWg9UJkMvj4hW_.
[79] B.Q. Li, J. Lin, W. Wang, Thermomechanical deflection of microcantilever beams in scanning force microscopes, J. Micromech. Microeng. 6 (3) (1996) 330.
[80] A. Chigullapalli, J.V. Clark, Modeling the Thermomechanical Interaction between an Atomic Force Microscope Cantilever and Laser Light Vol. 45257 (2012) 231–240.
[81] C. Weigel, V. Cherkasova, M. Holz, H.B. Phi, C. Görner Tenorio, B. Wilbertz, S. Strehle, Ultralow expansion glass as material for advanced micromechanical systems, Adv. Eng. Mater. 25 (9) (2023) 2201873.
[82] Y. Kim, Y.I. Yang, I. Choi, J. Yi, Effect of laser beam focusing point on AFM measurements, Korean J. Chem. Eng. 26 (2009) 496–499.
[83] D. Ma, J.N. Munday, Measurement of wavelength-dependent radiation pressure from photon reflection and absorption due to thin film interference, Sci. Rep. 8 (1) (2018) 15930.
[84] L.T. Dat, H.T. Huy, N.D. Vy, A theoretical study of deflection of AFM bimaterial cantilevers versus irradiated position, Commun. Phys. 28 (3) (2018).
[85] L. Landau, E. Lifshitz, Theory of Elasticity, Pergamon, London, 1959, p. 16.
[86] H. Ledbetter, Dynamic vs. static Young's moduli: a case study, Mater. Sci. Eng. A 165 (1) (1993) L9–L10.
[87] A. Goodwin, K.N. Marsh, W.A. Wakeham, Measurement of the Thermodynamic Properties of Single Phases, Elsevier, 2003, p. 311.
[88] https://www.azom.com/properties.aspx?ArticleID=53, last web access May 2025.
[89] https://www.tedpella.com/calibration_html/SEM_Magnification_Calibration_Standards.aspx#anchorG-1, last access November 2025.